

Formation of chlorite during thrust fault reactivation. Record of fluid origin and P–T conditions in the Monte Perdido thrust fault (southern Pyrenees)

B. Lacroix · D. Charpentier · M. Buatier ·
T. Vennemann · P. Labaume · T. Adatte ·
A. Travé · M. Dubois

Received: 4 April 2011 / Accepted: 30 December 2011 / Published online: 17 January 2012
© Springer-Verlag 2012

Abstract The chemical and isotopic compositions of clay minerals such as illite and chlorite are commonly used to quantify diagenetic and low-grade metamorphic conditions, an approach that is also used in the present study of the Monte Perdido thrust fault from the South Pyrenean fold-and-thrust belt. The Monte Perdido thrust fault is a shallow thrust juxtaposing upper Cretaceous–Paleocene platform carbonates and Lower Eocene marls and turbidites from the Jaca basin. The core zone of the fault, about 6 m thick, consists of intensely deformed clay-bearing rocks bounded by major shear surfaces. Illite and chlorite are the main hydrous minerals in the fault zone. Illite is oriented along cleavage planes while chlorite formed along shear veins (<50 μm in thickness). Authigenic chlorite provides essential information about the origin of fluids and their temperature. $\delta^{18}\text{O}$ and δD values of newly formed

chlorite support equilibration with sedimentary interstitial water, directly derived from the local hanging wall and footwall during deformation. Given the absence of large-scale fluid flow, the mineralization observed in the thrust faults records the P–T conditions of thrust activity. Temperatures of chlorite formation of about 240°C are obtained via two independent methods: chlorite compositional thermometers and oxygen isotope fractionation between cogenetic chlorite and quartz. Burial depth conditions of 7 km are determined for the Monte Perdido thrust reactivation, coupling calculated temperature and fluid inclusion isochores. The present study demonstrates that both isotopic and thermodynamic methods applied to clay minerals formed in thrust fault are useful to help constrain diagenetic and low-grade metamorphic conditions.

Keywords Clay minerals · Thrust fault · Thermometer · Stable isotope · Veins · P–T conditions

Communicated by F. Poitrasson.

B. Lacroix (✉) · D. Charpentier · M. Buatier
Chrono-Environnement, UMR 6249, Université de Franche
Comté-CNRS, 25000 Besançon, France
e-mail: brice.lacroix@unil.ch

B. Lacroix · T. Vennemann · T. Adatte
Institut de Minéralogie et Géochemie, Université de Lausanne,
1015 Lausanne, Switzerland

P. Labaume
Géosciences Montpellier, UMR 5243, Université Montpellier
2-CNRS, 34095 Montpellier, France

A. Travé
Departament de Geoquímica, Petrologia i Prospecció Geològica,
Universitat de Barcelona, 08028 Barcelona, Spain

M. Dubois
PBDS, UMR 8110, Université Lille 1, 59655 Lille, France

Introduction

With 18% of the worldwide hydrocarbon production, fold-and-thrust belts compose favorable sites of hydrocarbon generation, migration, and accumulation. Undiscovered oil and gas fields may still be expected in fold-and-thrust belts (Roure and Sassi 1995; Macgregor 1996; Alavi 2004), hence the interest in understanding the evolution of the foreland basin up to the development of a fold-and-thrust belt. To constrain the evolution of fold-and-thrust belts, it is essential to quantify the pressure and temperature (P–T) conditions of diagenesis and low-grade metamorphism. The chemical and isotopic compositions of minerals and their included fluids formed along fractures and fault planes can record the P–T conditions and/or the geothermal

gradients of such deformation in foreland basins (e.g., Rye and Bradbury 1988; Wiltchko et al. 2009; Parry and Blamey 2010). Clay minerals such as illite and chlorite have also been commonly used to quantify diagenetic and low-grade metamorphic conditions. In sedimentary rocks, the transition from smectite to illite and the measurement of illite crystallinity (IC) are among the most widely used methods to evaluate burial conditions (e.g., Kübler 1964; Frey 1987; Merriman et al. 1995; Lee and Lee 2001; Schwartz et al. 2009). Others have developed thermometers based on the chemical compositions of chlorite (Cathelineau and Nieva 1985; Cathelineau 1988; Hillier and Velde 1991; Vidal et al. 2005 and 2006 and Inoue et al. 2009). For example, Cathelineau and Nieva (1985) and Cathelineau (1988) propose an empirical calibration based on the correlation between the tetrahedral aluminum occupancy (Al^{IV}) and/or the octahedral vacancy as a function of temperatures deduced from fluid inclusions in fossil geothermal systems. Complementary studies demonstrated the effect of bulk-rock compositions on the chemical composition of chlorite (Hillier and Velde 1991; De Caritat et al. 1993; Zane et al. 1998, among others). More recently, Vidal et al. (2005, 2006) and Inoue et al. (2009) proposed a thermodynamic approach for calculating equilibrium conditions on the basis of chlorite compositions. Their methods take into account the variations of the mineralogy and the influence of physicochemical parameters such as fluid composition and redox conditions. Those geothermometers appear to be applicable to chlorite formed under diagenetic or low-grade metamorphic conditions during thrust fault activity. However, clay minerals can only be used as a proxy to estimate thrust fault P–T conditions if it can be clearly established that their formation is indeed related to the deformation. It is, therefore, important to trace the origin and behavior of clay minerals. During diagenesis and/or low-grade metamorphism, clay minerals can contribute to a slaty cleavage developed by passive rotation of detrital phyllosilicates or by mineralogical reactions and in situ neo-formation (Lee et al. 1986; Kreuzberger and Peacor 1988; Li et al. 1994; Ho et al. 2001; and Day-Stirrat et al. 2008).

The present study focuses on the northern part of the South Pyrenean fold-and-thrust belt (Figs. 1, 2), where stratigraphic, structural, and temperature conditions are relatively well-constrained (e.g., Séguret 1972; Mutti et al. 1988; Holl and Anastasio 1995; and Remacha and Fernandez 2003). Lacroix et al. (2011) demonstrated that the Monte Perdido thrust fault was formed during two stages. The first stage, related to the Monte Perdido thrust faulting, was associated to the formation of calcite-quartz shear veins. The second deformation stage corresponds to a fault reactivation involving newly formed clay minerals, chlorite in particular. However, the P–T conditions during this

second stage remain largely unknown. This paper focuses on the clay mineral assemblages from this fault formed during deformation and to evaluate their compositions as a low-grade geothermometers. The first part of the paper describes the behavior of clay minerals during deformation. The second part focuses on both the chemical and isotopic composition of chlorite in order to estimate their formation temperatures. The results are then used to derive the P–T conditions of thrusting and the geothermal gradient that affected the basin during deformation.

Geological setting

General background and study area

The Pyrenees correspond to a doubly vergent orogenic prism formed during the convergence between Iberia and Europe from the late Cretaceous to the early Miocene (e.g., Choukroune et al. 1990; Munoz 1992; Teixell 1998; and Beaumont et al. 2000).

From the north to the south, three main structural zones constitute the Pyrenean orogen (Fig. 1a). The North Pyrenean zone corresponds to a Mesozoic extensional basin system inverted and transported northward during the Pyrenean compression. To the south, the axial zone is defined by imbrications of south-verging thrust units in the Paleozoic basement (Fig. 1b). Southward, the thrust faults pass to a décollement in Triassic evaporites, at the base of the Mesozoic and Tertiary cover forming the South Pyrenean zone. Shortening caused by the Pyrenean deformation has been estimated to be about 165 km in the central Pyrenees (Beaumont et al. 2000) and 80 km in the western Pyrenees (Teixell 1998), about 70% of which was accumulated in the south-vergent thrust system.

The study area is located at the northern edge of the Jaca basin, which corresponds to the western part of the South Pyrenean zone (Fig. 1a). Above the Triassic décollement level, the stratigraphy of the Jaca Basin is given by Cenomanian to Santonian platform limestones followed by the upper Cretaceous–Paleogene syn-orogenic succession with, from bottom to top, Campanian to earliest Eocene platform carbonates, the Ypresian–Lutetian siliciclastic turbidites of the Hecho Group, and Bartonian to lower Oligocene coastal and continental deposits (e.g., Teixell 1996) (Fig. 1b). At the northern edge of the Jaca basin, Triassic evaporites are absent, and the Cretaceous limestones rest directly on the Paleozoic basement of the axial zone.

The present study focuses on the well-exposed Monte Perdido thrust fault, located in the north-eastern part of the Jaca Basin (Fig. 1b). It separates the Monte Perdido thrust unit from the underlying Gavarnie thrust unit (Fig. 1c). The

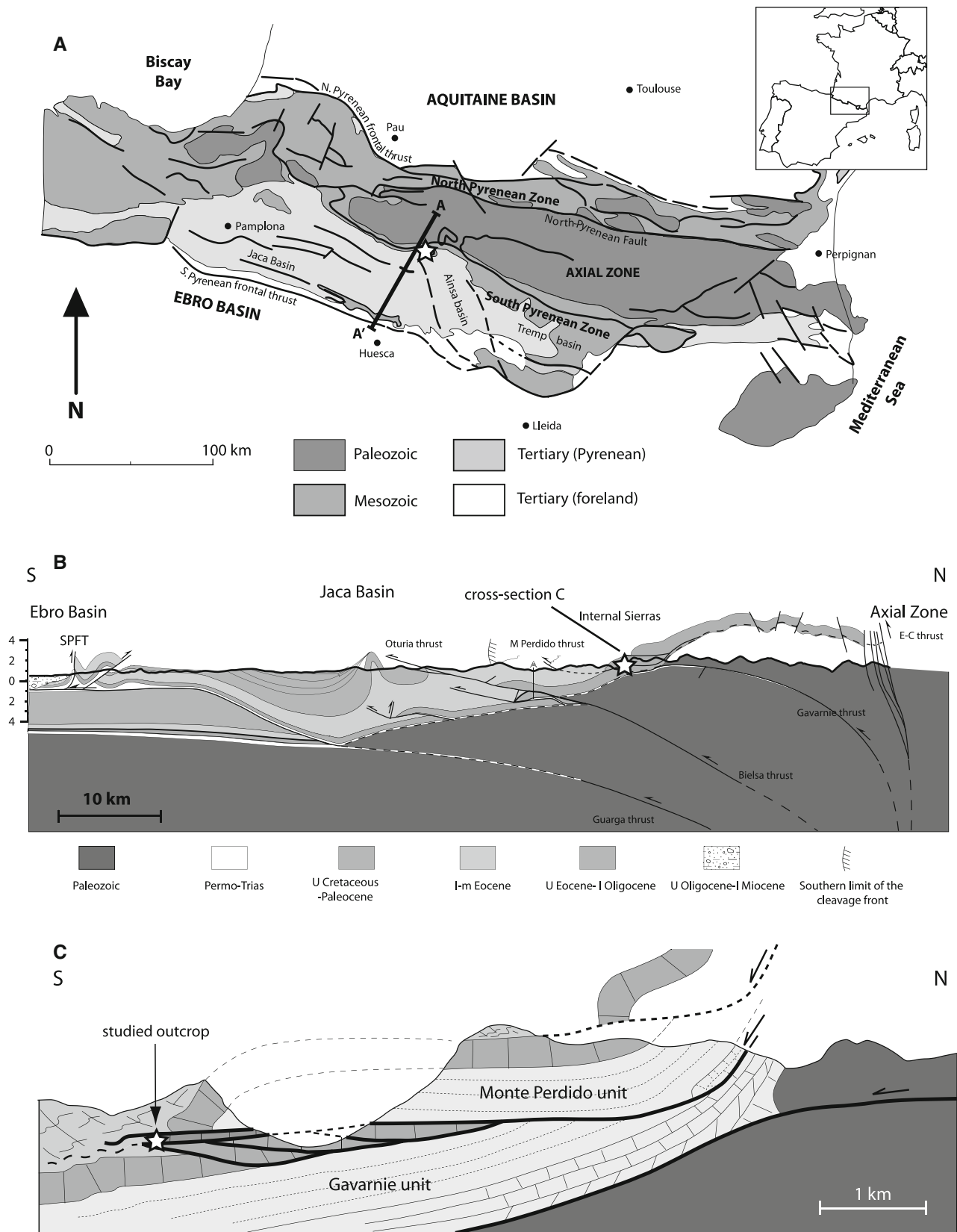


Fig. 1 a Structural map of Pyrenees with location of the studied area (modified from Lacroix et al. (2011)). b. A–A' cross-section of the South Pyrenean belt (modified from Meresse (2010)). c Detailed

cross-section from the Monte Perdido massif (modified from Séguret (1972)). Studied outcrop is given by the white star

Monte Perdido thrust activity is dated to the latest Lutetian to earliest Priabonian (47–37 Ma) (Teixell 1996). The northern part of the Monte Perdido thrust unit was folded and uplifted by the emplacement of the underlying Gavarnie basement thrust unit during the late Eocene-early Oligocene (Séguret, 1972; Teixell, 1996). Both units are characterized by a regional pressure-solution cleavage (Séguret 1972; Labaume et al. 1985; Teixell 1996; Oliva-Urcia et al. 2009) formed during their emplacement.

Outcrop description and sample location

One outcrop of the Monte Perdido sole thrust (Figs. 1c, 2) was studied in detail. The hanging wall is made up of the Alveolina limestone of the Monte Perdido thrust unit, and the footwall comprises the Hecho group turbidites (alternating sandstone and pelite layers) of the Gavarnie thrust unit (Fig. 2a).

The fault zone, about 6 m thick, consists of an interval of intensely deformed clay-bearing rocks bounded by major shear surfaces (Fig. 2a). The deformed sediment is markedly darker than the protolith. The presence of

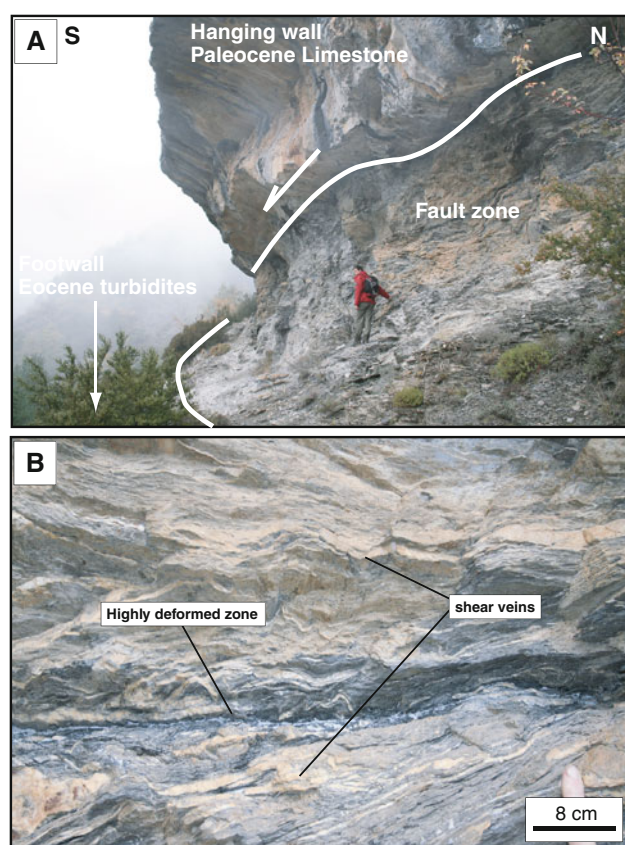


Fig. 2 Field photographs illustrating the studied section of the Monte Perdido thrust fault. **a** General view of the fault zone and the host sediments. **b** Detailed view of the highly deformed layer from the fault zone

decimetric, deformed sandstone lenses supports a development of the fault zone in the footwall turbidites. Deformation was accommodated by closely spaced cleavage associated with cm- to dm-spaced shear surface networks in a S–C (C′)-type structure. Calcite-quartz shear veins along the shear planes are abundant (Fig. 2b). Locally, the fault zone is strongly deformed, with more intense cleavage, folded and boudinaged veins adjacent to the fault (Fig. 2b). Additional details on the different types of structures in the fault zone are given in Lacroix et al. (2011). The cleavage orientation, the asymmetry of S–C structures, and steps along shear vein striation indicate a south-southwestward displacement (N315°E). The cleavage and shear veins are frequently deformed by centimetric folds with an axis oblique to the transport direction.

Although deformation principally occurs in the core zone, it also affects the hanging and footwall. In the hanging wall Alveolina limestone, the deformation is marked by stylolites and extension calcite veins. The footwall turbidites are deformed by cm- to dm-scale asymmetric, south-vergent folds with north-dipping axial plane cleavage. Extension veins are also present and crosscut the cleavage. The main orientation of cleavage outside the fault zone around N315°E is similar to that measured inside the fault zone. All kinematic markers thus indicate a tectonic transport toward the S–SW, sub-perpendicular to the regional N120 structural trend (Séguret 1972).

Detailed structural analysis focused on 20 samples along a vertical transect through the fault zone (Fig. 3). In this strongly deformed zone, calcite veins and dark foliated layers were sampled. Hanging wall Alveolina limestone and footwall Hecho group turbidites up to about 10–30 meters away from the deformation zone were also collected.

Methods

Microscopy

All samples were examined with a petrographic microscope on standard polished thin sections. Microstructures and mineral species were identified with a JEOL JSM5600 scanning electron microscope coupled with a FONDIS energy dispersive analyzer (EDS) at the University of Franche Comté (Besançon). Images were obtained with backscattered electrons at 20 kV.

X-Ray diffraction

The bulk-rock and clay mineralogy of samples from host rock and foliated layers was analyzed with a SCINTAG

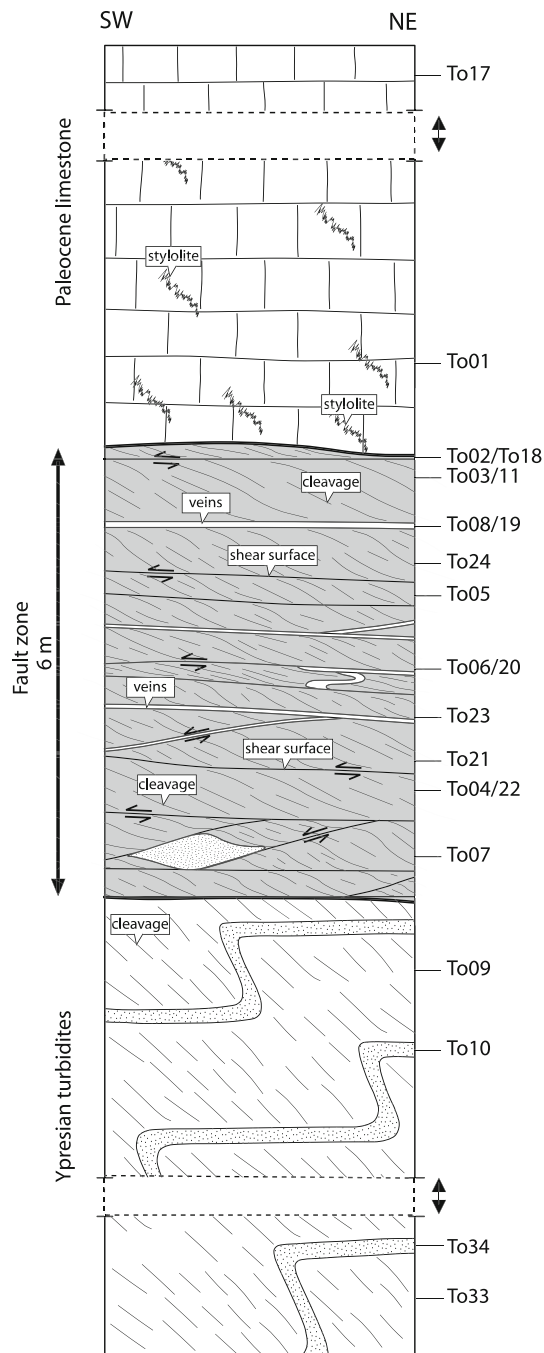


Fig. 3 Schematic diagram of the structural organization in the studied fault zone (modified from Lacroix et al. 2011). The sample locations are labeled as ToXX. Note: the presence of deformation structures such as shear surfaces, cleavage, stylolites, and veins

XRD 2000 diffractometer at the Geological Institute of Neuchatel, Switzerland, following the procedures outlined by Kübler (1987) and Adatte et al. (1996). The XRD diffractometer was operated at 45 kV and 40 mA and equipped with a Cu tube.

The bulk-rock mineralogy of 15 samples was analyzed by X-ray diffraction obtained between $5^{\circ} 2\theta$ and $60^{\circ} 2\theta$ with a step size of $0.03^{\circ} 2\theta$ and a goniometer speed of $0.5^{\circ}/\text{min}$, 45 kV/18 mA.

Clay mineral fractions from 15 samples were extracted from powdered chips that were mixed with de-ionized water (pH 7–8) and agitated. The carbonate fraction was removed with the addition of HCl 10% (1.25 N) at room temperature until all the carbonate was dissolved. The samples were disaggregated using an ultrasound for 3 min. The insoluble residues were washed and centrifuged until a neutral suspension was obtained (pH 7–8). Separation of different grain size fractions ($<2 \mu\text{m}$ and $2\text{--}16 \mu\text{m}$) was obtained by the timed settling method based on Stokes law. The selected fractions were then deposited onto a glass plate and air-dried at room temperature. XRD analyses of oriented clay samples were made after air drying at room temperature and after saturation of the samples with ethylene glycol. The intensities of selected XRD peaks characterizing each clay mineral in the size fraction (e.g., chlorite, mica) were measured for a semi-quantitative analysis of the proportion of clay minerals present in the size fractions $<2 \mu\text{m}$ and $2\text{--}16 \mu\text{m}$.

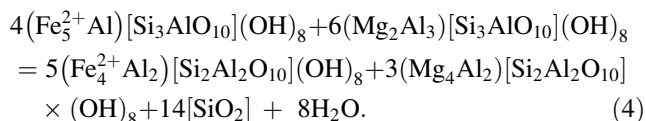
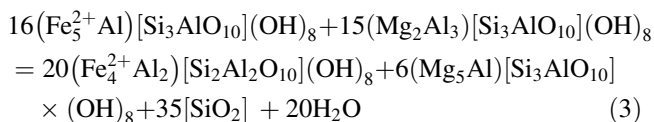
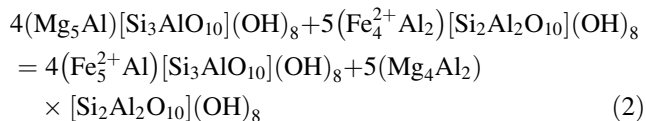
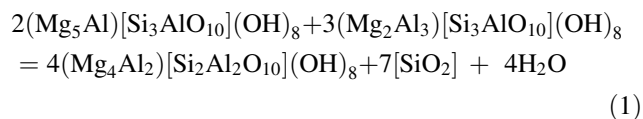
Chlorite analysis

The chemical composition (Si, Fe, Mg, Al, Ti, K, Ca, and Na) of selected chlorites from the highly deformed core zone of the fault was analyzed using a CAMECA model SX100 electron microprobe at the University of Montpellier equipped with five X-ray spectrometers on 2 carbon-coated thin sections. The microprobe was operated using 20 kV of excitation potential, 10 nA of current intensity, and a beam diameter of $3 \mu\text{m}$. The standards used were Wollastonite (Si, Ca), Fe_2O_3 (Fe), Forsterite (Mg), Al_2O_3 (Al), TiO_2 (Ti), Orthoclase (K), and Albite (Na).

Temperatures were estimated using the composition of chlorites and following the method of Vidal et al. (2005, 2006) and of Inoue et al. (2009). Vidal et al. (2006) proposed a thermodynamic model for Fe-Mg partitioning in aluminous trioctahedral chlorites ($\text{Si} < 3 \text{ p.f.u.}$). Four end-members were chosen:

- clinocllore (Mg_5Al)[$\text{Si}_3\text{AlO}_{10}$](OH) $_8$,
- daphnite ($\text{Fe}_5^{2+}\text{Al}$)[$\text{Si}_3\text{AlO}_{10}$](OH) $_8$,
- amesite ($\text{Mg}_4 \text{Al}_2$)[$\text{Si}_2\text{Al}_2\text{O}_{10}$](OH) $_8$ and ($\text{Fe}_4^{2+} \text{Al}_2$)[$\text{Si}_2\text{Al}_2\text{O}_{10}$](OH) $_8$
- sudoite (Mg_2Al_3)[$\text{Si}_3\text{AlO}_{10}$](OH) $_8$.

The choice of these components allows for a description of the Fe-Mg, Tschermak, and dioctahedral-trioctahedral substitutions occurring in trioctahedral chlorites. Using these end-members, four reactions (two independent) can be written for chlorite-quartz-water assemblages:



The temperatures of equilibrium (Eq. 1)–(Eq. 4) depend on the activity and, therefore, the proportions of the clinocllore, daphnite, sudoite, and amesite end-members in chlorite. These temperatures can be calculated using the condition of thermodynamic equilibrium:

$$0 = \sum_j v_j \Delta_a G_j^{P,T} - RT \ln K, \quad (5)$$

where v_j is the stoichiometric reaction coefficient, $\Delta_a G_j^{P,T}$ is the apparent Gibbs free energy of formation (Berman 1988), and K is the equilibrium constant, which can be written as:

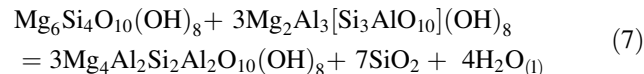
$$K = \prod_j (a_{\text{ideal}} \gamma_m)^{v_j}, \quad (6)$$

where a_{ideal} is the ideal part of the activity and γ_m is the activity coefficient.

As is the case for other phyllosilicates, substitution of Al^{3+} for Fe^{3+} also occurs in chlorite. Fe^{3+} can influence the number of vacancies in the chlorite structure, and the presence of Fe^{3+} may affect the activity of the chlorite end-members. A simultaneous estimation of Fe^{3+} in chlorite and equilibrium temperature for the Chl-Qtz-H₂O assemblage can be done at given pressure of 1 kbar with a temperature difference of 20°C and $a_{\text{H}_2\text{O}}$ using a temperature scatter of 20°C and a criterion based on the convergence of equilibria (Eq. 1)–(Eq. 4) (Vidal et al. 2005).

Inoue et al. (2009) substituted the end-member component of chlorite solid solution from clinocllore adopted by Vidal et al. (2001) for Al-free chlorite with a serpentine composition, so that the chosen end-member components of the solid solution are more suitable for describing the wide range of elemental substitutions in low-temperature chlorites. Indeed, it is known that low-T chlorites have higher Si contents and octahedral vacancies and lower Fe + Mg contents for a similar Al_2O_3 content compared to higher-grade metamorphic chlorites (e.g., Hillier and Velde

1991). Using the calibrated thermodynamic properties, they estimated the formation temperatures of chlorite + quartz assemblage that is expressed by the reactions:



$$\text{at: } T \text{ (}^\circ\text{C)} = \frac{1}{(0.00293 - 5.13 \times 10^{-4}x + 3.904 \times 10^{-5}x^2)} - 273 \quad (8)$$

where

$$x = \log K' = 3 \log a_{\text{crdp}}^{\text{ideal}} - 3 \log a_{\text{sud}}^{\text{ideal}} - \log a_{\text{Adeh}}^{\text{ideal}} \quad (9)$$

Here, random mixing of cations and vacancies in the six octahedral sites of chlorite solid solution is assumed. In both models, it is also assumed $a_{\text{H}_2\text{O}} = 1$. The assumption of $a_{\text{H}_2\text{O}} = 1$ is reasonable in diagenetic to low-grade metamorphic and hydrothermal environments related to the chlorite formation (Inoue et al. 2009). However, we should keep in mind that if $a_{\text{water}} < 1$, the temperature of chlorite formation will be overestimated.

Stable isotope analysis

The oxygen isotope composition (^{16}O , ^{18}O) of the clay fractions (<2 μm), chlorite veins, and quartz veins were measured on 6 selected samples at the University of Lausanne, using a method similar to that described by Sharp (1990) and Rumble and Hoering (1994) and described in more detail in Kasemann et al. (2001). Clay fractions (<2 μm) were extracted using Stokes law and particle settling in water, on samples from host sediments (To17 and To34) and from the fault zone (To06 and To19). Quartz from To11 (equivalent to To06 and To19) was extracted by crushing and hand-picking under a binocular microscope. Because of the very small size of the chlorite veins in the studied samples, extraction of chlorite was possible in only two samples (To11 and To21) equivalent to To06 and To19. In these samples, chlorite is generally associated with calcite veins. Thin slices of the rocks were cut normal to the cleavage and shear planes before chlorite was extracted. The chlorite fraction was then removed by applying several cycles of disaggregation by ultrasound in water and calcite dissolution by HCl. Once the calcite was dissolved, additional disaggregation was applied to samples by traditional crushing. Chlorite crystals were then picked under a binocular microscope.

Prior to oxygen extraction, all samples were dried in an oven for 12 h at 150°C. Between 0.5 to 2 mg of sample was loaded onto a small Pt sample holder and pumped out to a vacuum of about 10^{-6} mbar. After pre-fluorination of the sample chamber overnight, the samples were heated with a CO₂-laser in 50 mbars of pure F₂. Excess F₂ is

separated from the O₂ by conversion to Cl₂ using KCl held at 150°C. The extracted O₂ is collected on a molecular sieve and subsequently expanded into the inlet of a Finnigan MAT 253 isotope ratio mass spectrometer. Oxygen isotope compositions are given with the standard δ -notation, expressed relative to VSMOW in permil (‰). Replicate oxygen isotope analyses of the standard used (NBS-28 quartz; or LS-1 Qtz) has an average precision of $\pm 0.1\text{‰}$ for $\delta^{18}\text{O}$. The accuracy of $\delta^{18}\text{O}$ values is better than 0.2‰, compared to accepted $\delta^{18}\text{O}$ values for NBS-28 of 9.64‰.

Measurements of the hydrogen isotope compositions of minerals were made using high-temperature (1,450°C) reduction methods with He-carrier gas and a TC-EA linked to a Delta Plus XL mass spectrometer from Thermo-Finnigan on 2–4 mg sized samples according to a method adapted after Sharp et al. (2001). The results are given in the standard δ -notation, expressed relative to VSMOW in permil (‰). The precision of the in-house kaolinite and G1 biotite standards for hydrogen isotope analyses was better than $\pm 2\text{‰}$ for the method used; all values were normalized using a value of -125‰ for the kaolinite standard and -65‰ for NBS-30.

Results

Petrography and microstructures

Host rocks

Host sediments are composed of Alveolina limestone in the hanging wall and turbidites from the Hecho group in the footwall. The Alveolina limestone is a wackstone comprising bioclasts and disseminated detrital quartz and calcite grains supported by a micritic calcite matrix (Fig. 4a). Disseminated pyrite crystals are also present. XRD analyses on bulk-rock powders indicate dominant proportions of calcite and quartz, whereas illite and chlorite are present in smaller amounts. Feldspars are absent except for sample To18 (Table 1).

The Hecho group turbidites are composed of alternate sandstone (Fig. 4b) and centimeter- to decimeter-thick pelite layers (Fig. 4c). A detailed petrographic description of the Hecho group sandstones is given in Caja et al. (2009). In sandstones, the major phase is detrital quartz (Fig. 4b). Detrital grains are cemented by well-crystallized sparitic calcite. Detrital chlorite and illite occur in the clay fraction but in small amounts. Pelites also contain detrital quartz and clay minerals (chlorite and illite) cemented by calcite. SEM observations (Fig. 4d, e) indicate that clay minerals are abundant in the matrix. Along styloliths, illite-chlorite aggregates of about 40 μm are locally present and could be mechanically reoriented (Fig. 4e). Detrital quartz grains and calcite cements have local dissolution marks on their

boundaries, as shown in Fig. 4d. XRD analyses on pelitic bulk rocks indicate a dominance of calcite and quartz with lesser illite and chlorite, whereas feldspars are absent (Table 1).

Fault zone

The core of the fault zone is characterized by the presence of a pervasive cleavage, mineralized veins and folding developed during three main stages of deformation (Lacroix et al. 2011). The first stage structures comprise a pervasive cleavage affecting the clay-rich sediment and calcite shear veins referred to as shear veins 1 (S_{V1}). These structures are often affected by a second stage of deformation with two types of veins referred to as extension veins 2 (E_{V2}) and shear veins 2 (S_{V2}) and folding. A late stage of deformation is marked by extension veins 3 (E_{V3}), which correspond to networks of irregular fractures filled with blocky to elongated calcite crystals. The E_{V3} veins result from the dilatancy of pre-existing weakness structures such as cleavage, vein boundaries and shear surfaces. They were probably formed under high fluid pressure during the late exhumation of the massif. Figure 5a presents the different structures observed in the highly deformed fault zone. The S_{V1} veins correspond to blocky calcite-quartz shear veins. They are folded and crosscut by the E_{V2} and S_{V2} veins (Fig. 5a, b) (detailed descriptions are available in Lacroix et al. 2011). The E_{V2} veins are extension (boudinage) veins opened across S_{V1} and filled by elongated calcite and quartz in similar proportions (Fig. 5a and B). The interdigitation of both minerals indicates that they precipitated contemporaneously (Durney and Ramsay 1973; Kirschner et al. 1995). The S_{V2} veins occur in the deformed sediment and correspond to micro-shear veins filled with phyllosilicates (Fig. 5b–d). In Fig. 5c, microstructure observed on thin sections reveals that the S_{V2} veins are developed along shear surfaces (C and C') of the S–C pattern. Locally, chlorite can surround calcite ribbons parallel to the vein wall. Each calcite ribbon is formed by a lateral succession of rhomb-shaped veinlets (Fig. 5d) corresponding to incremental pull-apart openings following a crack-seal mechanism along an extensional relay zone. Obliquity between the shear planes and the cleavage gives the sense of shear (top to the south). Figure 5b shows that a new axial plane cleavage is formed in the hinge of isoclinal folds affecting S_{V1} veins.

Clay mineralogy

XRD analysis

XRD analyses have been made on the clay fractions (<2 and 2–16 μm) of the footwall and hanging wall as well as of the highly deformed fault zone (Fig. 6 and Table 2).

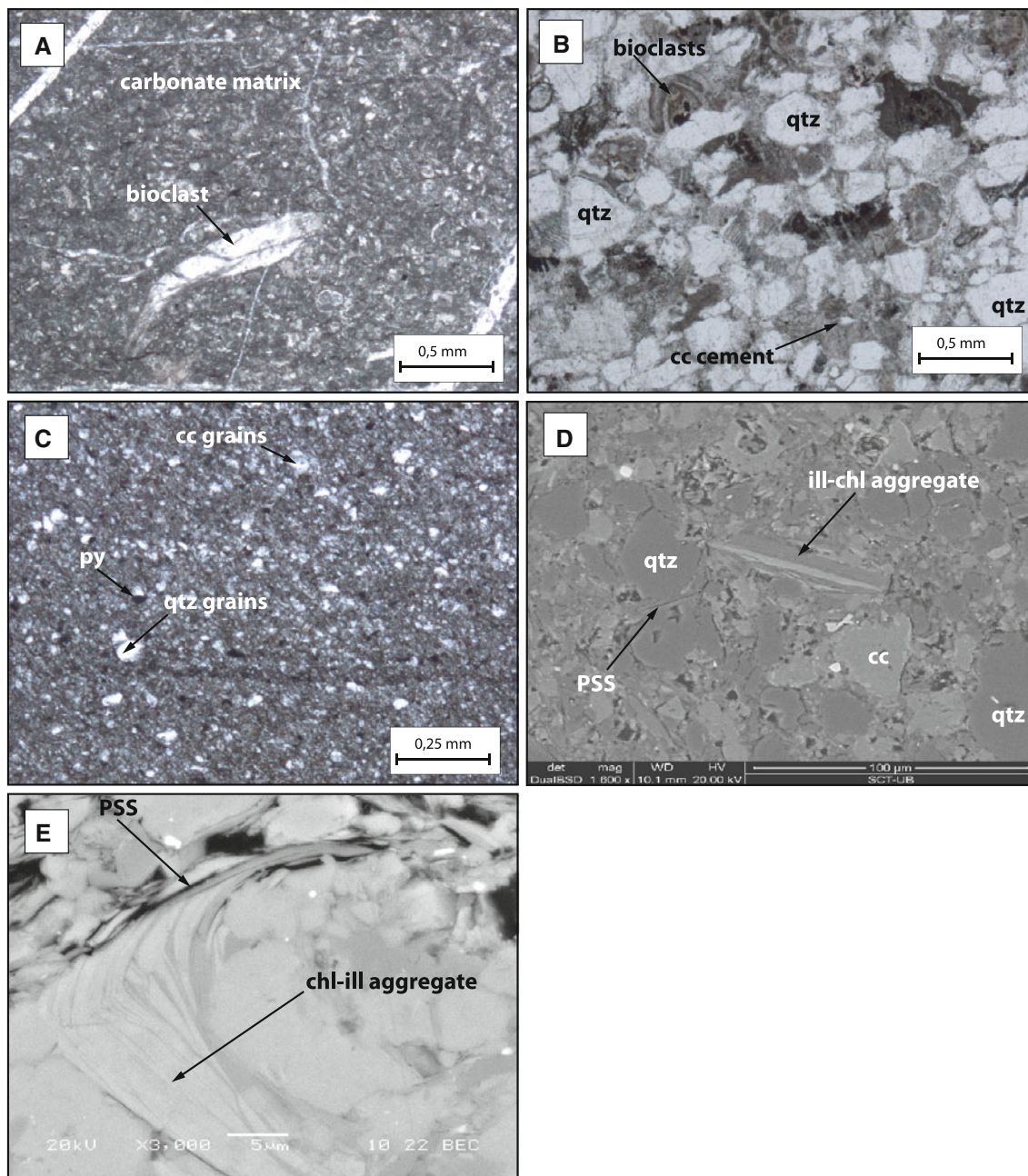


Fig. 4 Optical (**a**, **b**, **c**) and backscattered scanning electron micrographs (**d** and **e**) of thin sections. **a** Limestone from hanging wall (sample To17). **b** Sandstone from the Hecho group turbidites (sample To31). **c** Pelitic layer from the Hecho group turbidites (sample To31). **d** and **e** Pelite from Hecho group turbidite presenting detrital illite/

chlorite stacks in the matrix. Note that, small detrital stacks are reoriented along pressure-solution surfaces (sample To31). *Cc*, calcite; *qtz*, quartz; *PSS*, pressure-solution surfaces; *py*, pyrite; *ill*, illite; and *chl*, chlorite

An illite-chlorite assemblage is present in both the hanging wall (limestone) and the footwall (pelite + sandstone). XRD also confirms that an illite-chlorite assemblage is present in all samples from the fault rocks. Illite is dominant in the hanging wall limestone, whereas footwall pelite and sandstones contain chlorite and illite in similar proportions. The absence of expanded layer clays (i.e.

smectite) in the $<2 \mu\text{m}$ fraction has been confirmed by XRD analyses of glycolated clay fractions.

Semi-quantitative proportions of chlorite related to illite have been determined using the ratio $002_{\text{chlorite}}/(002_{\text{chlorite}} + 002_{\text{illite}})$ ($C/(I+C)$) peak intensity (Table 2). The ratio for the $<2 \mu\text{m}$ and 2–16 μm fraction is similar within limestone, ranging from 0.29 to 0.39. In pelite and

Table 1 Bulk-rock mineralogy determined by XRD

Samples	Lithology	Bulk rock	Bulk rock				
			Calcite	Quartz	Illite	Chlorite	Feldspath
To17	Limestone	Hanging wall	****	*	–	–	
To01	Limestone	Hanging wall	****	*	–	–	
To02	Deformed limestone	Fault zone	****	**	–	–	
To18	Deformed limestone	Fault zone	****	**	–	–	*
To19	Deformed marl	Fault zone	***	****	*	**	
To24	Deformed marl	Fault zone	***	***	*	**	
To05	Deformed marl	Fault zone	***	***	*	**	
To11	Deformed marl	Fault zone	***	****	*	**	
To20	Deformed marl	Fault zone	****	****	**	**	
To23	Deformed marl	Fault zone	*	****	***	**	
To21	Deformed marl	Fault zone	***	****	*	**	
To22	Deformed marl	Fault zone	***	***	**	**	
To30	Pelite	Footwall	***	****	**	**	
To31	Sandstone	Footwall	**	****	*	*	
To34	Pelite	Footwall	***	***	**	**	

**** very abundant, *** abundant, ** present, * rare, –trace

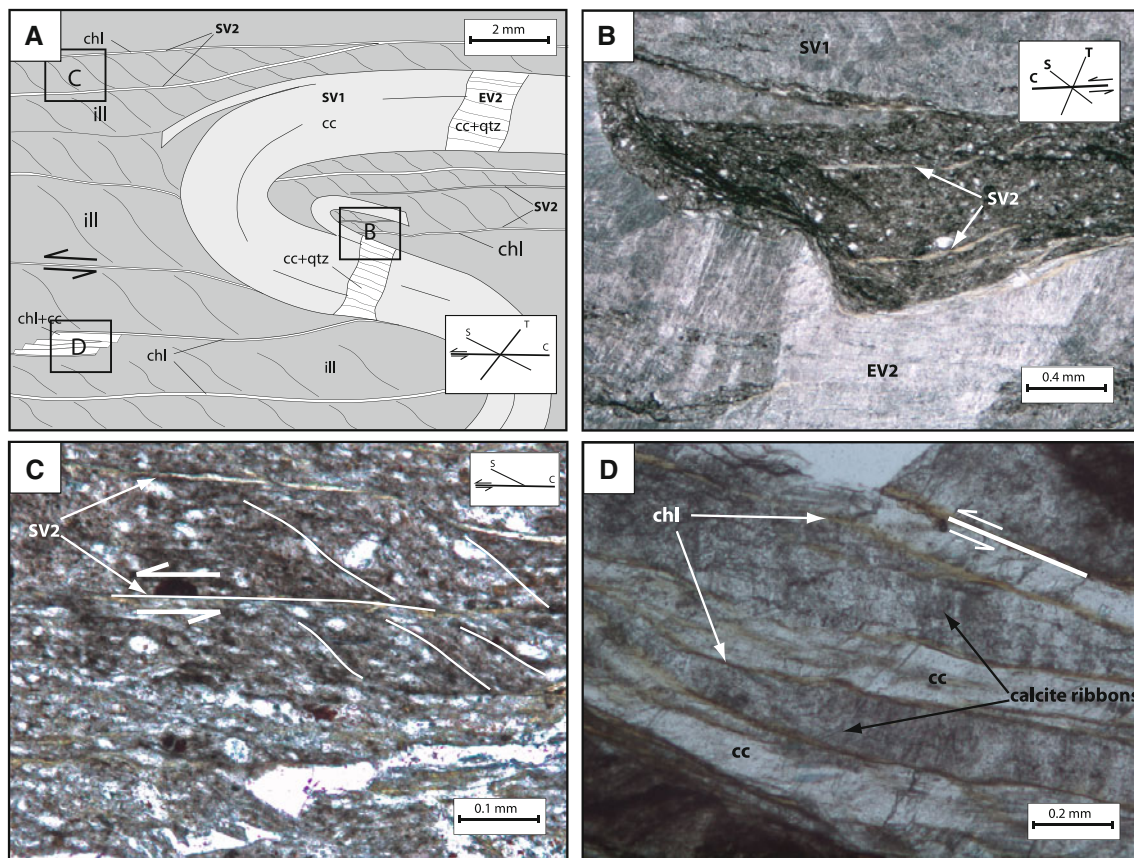
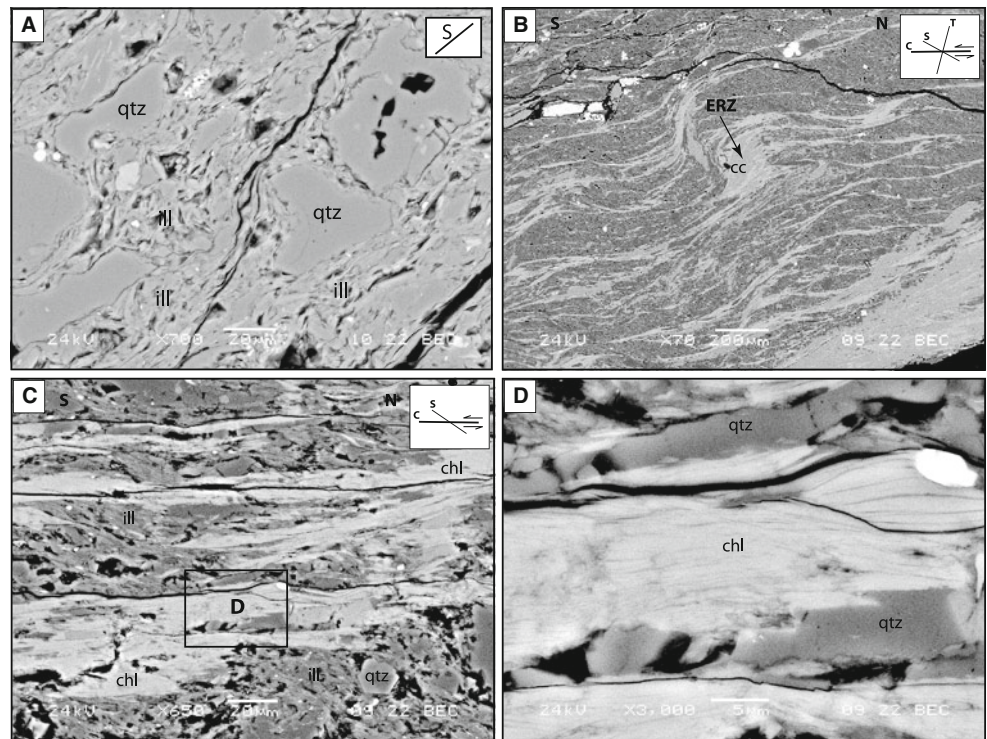


Fig. 5 Microstructures observed in the Monte Perdido thrust fault by optical and backscattered electron microscopy. **a** Schematic diagram from thin section showing all microstructures observed. **b** Late deformation affecting calcite shear veins (S_{V1}) (sample To11). This deformation is characterized by the development of folds, E_{V2} boudinage veins in S_{V1} calcite shear veins and S_{V2} chlorite micro-

shear veins in the matrix. **c** Relationship between cleavage and micro-shear surfaces defining a $S-C(C')$ -type structure (sample To21). **d** Detail of late S_{V2} chlorite shear veins with presence of calcite in extensional relay zone (sample To11). *Cc*, calcite; *qtz*, quartz; *chl*, chlorite; *ill*, illite; *C*, shear surfaces; and *S*, cleavage

Fig. 7 Backscattered scanning electron microscopy images illustrating the presence of illite along cleavage and the chlorite micro-shear veins development (sample To19). **a** Details of illite cleavage and corroded detrital quartz grains suggesting a local pressure solution of quartz. **b** General view of chlorite S_V2 veins (sample To19). Shear surfaces are connected to extensional relay zone (ERZ) in which calcite (cc) precipitated. **c** S_V2 veins defining shear bands. The relationship between illite cleavage (S) and shear bands suggests a south-southwest kinematic. **d** Details of S_V2 veins where chlorite crystals are elongated parallel to shear surfaces. Cc calcite, qtz quartz, chl chlorite, illite illite, ERZ extensional relay zone



be attributed to a higher iron content in the newly formed chlorite (Moore and Reynolds 1997 and Solum and Van der Pluijm 2009).

The illite crystallinity index (IC) has also been determined on the $<2\ \mu\text{m}$ fractions using the XRD patterns. Values range from 0.17 to 0.27 (Table 2) for the host rocks. The IC index ranges from 0.16 to 0.35 in the deformed sediments (Table 2). Samples To11, To19, and To20, which present the highest IC values, correspond to the more intensely deformed zone where folds, E_V2 and S_V2 veins, and newly formed cleavage in fold hinges are present.

SEM observations

Deformed marls from the fault core observed at higher magnification by SEM show very small oriented illite crystals ($<2\ \mu\text{m}$) defining the foliation (Fig. 7a). Detailed SEM observations of highly deformed fault zone samples indicate that the S_V2 shear veins are filled with chlorite, whereas the clay-rich matrix has lower contrast demonstrating higher abundance of illite (Fig. 7b). Figure 7c, d indicate chlorite lamellae filling S_V2 veins, which are about 5–10 μm in diameter. This observation is consistent with XRD data indicating higher abundance of chlorite in the 2–16 μm fraction compared to the $<2\ \mu\text{m}$ fraction.

SEM images show that calcite rhomb-shaped veinlets are locally observed along extensional relay zone among chlorites (Fig. 7b). Chlorites occur as lamellae oriented

parallel to the shear surfaces (Fig. 7c, d). This demonstrates that chlorite cement precipitated coevally with the shear displacement.

Microprobe analysis

The chemical composition of syntectonic chlorites was determined from microprobe analyses on chlorite from S_V2 bearing veins (samples To11 and To21). The results presented in Table 3 and Fig. 8 show that chlorites from the two studied samples have very similar compositions. They are iron-rich chlorite (between 2.26 and 2.63 a.p.f.u). Slightly higher Mg content is observed in sample To21. The ternary plot presented in Fig. 8 indicates that the studied chlorite compositions can be defined in terms of the end-members determined by Vidal et al. (2005, 2006), as well as those defined by Inoue et al. (2009).

The temperatures of chlorite formation were determined using the thermodynamic thermometer from Vidal et al. (2005, 2006), and from Inoue et al. (2009) (Table 3).

Stable isotope compositions

$\delta^{18}\text{O}$ and δD values (Table 4 and Fig. 9) of $<2\ \mu\text{m}$ fractions were measured on one sample from the hanging wall Alveolina limestones (sample To17), two samples from the fault zone (samples To19 and To06) and one sample from the footwall pelite (sample To34). In the hanging wall and footwall, the $\delta^{18}\text{O}$ values of the $<2\ \mu\text{m}$ fraction vary

Table 3 Chemical compositions of chlorite obtained by microprobe analysis

Samples	To11																
	3	5	6	9	10	12	13	15	19	26	27	28	33	34	35	41	46
SiO ₂	25.59	25.55	26.34	26.18	25.3	25.37	25.86	26.08	25.67	26.26	25.71	25.56	25.19	26.07	25.64	25.6	25.78
TiO ₂	0.01	0.03	0.04	0.02	0.00	0.01	0.03	0.03	0.03	0.05	0.04	0.02	0.09	0.05	0.02	0.03	0.02
Al ₂ O ₃	23.42	23.68	24.3	23.62	24.25	23.97	24.05	23.86	23.32	23.63	23.49	23.43	23.55	23.79	23.52	22.99	23.67
FeO	28.94	28.66	28.84	28.95	28.51	29.56	28.75	29.27	29.12	29.07	29.2	29.27	29.27	29.28	29.64	29.24	28.96
MnO	0.01	0.00	0.01	0.01	0.02	0.02	0.00	0.02	0.02	0.03	0.02	0.03	0.04	0.04	0.03	0.02	0.00
MgO	9.33	9.08	9.11	9.43	9.53	9.21	9.35	9.57	9.48	9.18	8.76	9.27	9.19	9.04	8.95	9.13	9.04
CaO	0.19	0.11	0.13	0.12	0.07	0.05	0.21	0.13	0.11	0.11	0.12	0.21	0.08	0.2	0.12	0.17	0.17
Na ₂ O	0.01	0.01	0.04	0.01	0.02	0.00	0.02	0.00	0.04	0.00	0.00	0.00	0.01	0.00	0.01	0.04	0.00
Total	87.65	87.17	88.92	88.34	87.7	88.2	88.27	88.96	87.79	88.33	87.34	87.79	87.42	88.47	87.93	87.22	87.64
14 oxygens																	
Si	2.73	2.73	2.76	2.76	2.69	2.7	2.73	2.74	2.73	2.77	2.75	2.72	2.7	2.75	2.73	2.75	2.74
Al ^{IV}	1.27	1.27	1.24	1.24	1.31	1.3	1.27	1.26	1.27	1.23	1.25	1.28	1.3	1.25	1.27	1.25	1.26
Al ^{VI}	1.67	1.72	1.75	1.7	1.73	1.7	1.72	1.69	1.66	1.71	1.72	1.67	1.68	1.71	1.69	1.65	1.71
Fe	2.58	2.57	2.52	2.55	2.53	2.63	2.54	2.57	2.59	2.56	2.61	2.61	2.62	2.58	2.64	2.62	2.58
Mn	0.00	0.00	0.00	0.00	0.00	0.00	0.00	0.00	0.00	0.00	0.00	0.00	0.00	0.00	0.00	0.00	0.00
Mg	1.48	1.45	1.42	1.48	1.51	1.46	1.47	1.5	1.51	1.44	1.4	1.47	1.47	1.42	1.42	1.46	1.43
Ca	0.04	0.03	0.03	0.03	0.02	0.01	0.05	0.03	0.03	0.03	0.03	0.05	0.02	0.05	0.03	0.04	0.04
Na	0.00	0.00	0.01	0.00	0.00	0.00	0.00	0.00	0.01	0.00	0.00	0.00	0.00	0.00	0.00	0.01	0.00
T° C Vidal	248	241	224	228	279	279	248	245	246	218	231	254	268	234	249	237	237
XFe ³⁺	0.09	0.08	0.10	0.12	0.11	0.11	0.07	0.09	0.10	0.13	0.10	0.08	0.05	0.10	0.08	0.12	0.09
T° C Inoue																	
XFe ³⁺ Vidal	244	239	218	226	282	285	240	243	247	218	228	250	270	226	246	235	232
XFe ³⁺ = 0	266	259	234	251	293	301	255	269	275	240	250	273	292	245	271	261	252
XFe ³⁺ = 0.1	248	240	219	232	268	272	239	248	253	223	231	254	267	229	249	242	235
XFe ³⁺ = 0.2	233	227	208	219	253	255	227	233	237	211	219	239	251	217	234	228	222

Table 3 continued

Samples	To21	1	2	4	6	9	11	16	17	18	19	20	21	22	23	27	29	31	32
SiO ₂	26.39	25.97	26.08	26.78	26.32	26.01	26.45	26.03	25.77	26.18	26.01	26.12	26.57	25.89	26.05	26.86	26.55	26.32	
TiO ₂	0.03	0.02	0.01	0.03	0.01	0.04	0.03	0.01	0.04	0.01	0.02	0.01	0.04	0.02	0.03	0.02	0.00	0.03	
Al ₂ O ₃	23.38	23.16	23.05	23.36	22.15	22.87	23.56	22.77	22.86	23.19	23.45	23.22	22.75	23.07	23.15	23.08	23.12	22.98	
FeO	26.64	26.35	26.24	26.34	25.85	26.55	26.72	26.58	26.18	26.8	26.82	26.5	25.84	26.67	26.51	25.77	26.14	26.23	
MnO	0.02	0.02	0.02	0.01	0.02	0.01	0.02	0.00	0.01	0.03	0.01	0.02	0.03	0.03	0.02	0.02	0.01	0.02	
MgO	11.3	11.8	11.75	11.41	11.00	11.49	11.58	11.73	11.48	11.54	11.84	11.58	11.69	11.54	11.35	11.24	11.7	11.74	
CaO	0.04	0.04	0.03	0.02	0.11	0.14	0.03	0.02	0.02	0.16	0.06	0.04	0.1	0.03	0.05	0.14	0.04	0.06	
Na ₂ O	0.03	0.00	0.00	0.02	0.02	0.00	0.02	0.00	0.02	0.00	0.01	0.01	0.00	0.01	0.01	0.06	0.02	0.00	
Total	87.83	87.36	87.18	87.97	85.48	87.1	88.41	87.14	86.38	87.91	88.22	87.5	87.02	87.26	87.17	87.2	87.58	87.38	
14 oxygens																			
Si	2.77	2.74	2.76	2.8	2.83	2.76	2.76	2.76	2.75	2.75	2.72	2.75	2.8	2.74	2.76	2.82	2.79	2.77	
Al ^{IV}	1.23	1.26	1.24	1.2	1.17	1.24	1.24	1.24	1.25	1.25	1.28	1.25	1.2	1.26	1.24	1.18	1.21	1.23	
Al ^{VI}	1.66	1.62	1.63	1.67	1.64	1.61	1.65	1.6	1.63	1.62	1.62	1.64	1.63	1.62	1.64	1.68	1.65	1.62	
Fe	2.34	2.33	2.32	2.3	2.32	2.35	2.33	2.36	2.34	2.35	2.35	2.34	2.28	2.36	2.35	2.26	2.29	2.31	
Mn	0.00	0.00	0.00	0.00	0.00	0.00	0.00	0.00	0.00	0.00	0.00	0.00	0.00	0.00	0.00	0.00	0.00	0.00	
Mg	1.77	1.86	1.85	1.78	1.76	1.81	1.8	1.85	1.83	1.81	1.85	1.82	1.84	1.82	1.79	1.76	1.83	1.84	
Ca	0.01	0.01	0.01	0.01	0.03	0.03	0.01	0.00	0.00	0.03	0.01	0.01	0.02	0.01	0.01	0.03	0.01	0.01	
Na	0.01	0.00	0.00	0.00	0.00	0.00	0.00	0.00	0.00	0.00	0.00	0.00	0.00	0.00	0.00	0.01	0.00	0.00	
T° C Vidal	234	258	248	218	204	249	241	249	248	252	273	249	221	257	246	201	227	239	
XFe ³⁺	0.15	0.12	0.14	0.18	0.23	0.14	0.14	0.15	0.14	0.13	0.09	0.13	0.20	0.12	0.13	0.22	0.18	0.16	
T° C Inoue																			
XFe ³⁺ Vidal	231	259	248	215	201	244	240	251	248	247	275	248	215	258	242	197	225	235	
XFe ³⁺ = 0	266	299	290	247	229	280	278	299	288	282	311	287	247	298	279	220	263	273	
XFe ³⁺ = 0.1	243	271	262	227	213	258	253	268	261	260	281	260	229	270	254	206	240	250	
XFe ³⁺ = 0.2	229	253	245	214	200	241	238	249	244	243	262	243	215	252	238	195	225	234	

Atomic proportions were calculated on the basis of 28 negative charges (i.e., 14 oxygens). Temperature calculation and Fe oxidation states follow the models of Vidal et al. (2005) and Inoue et al. (2009)

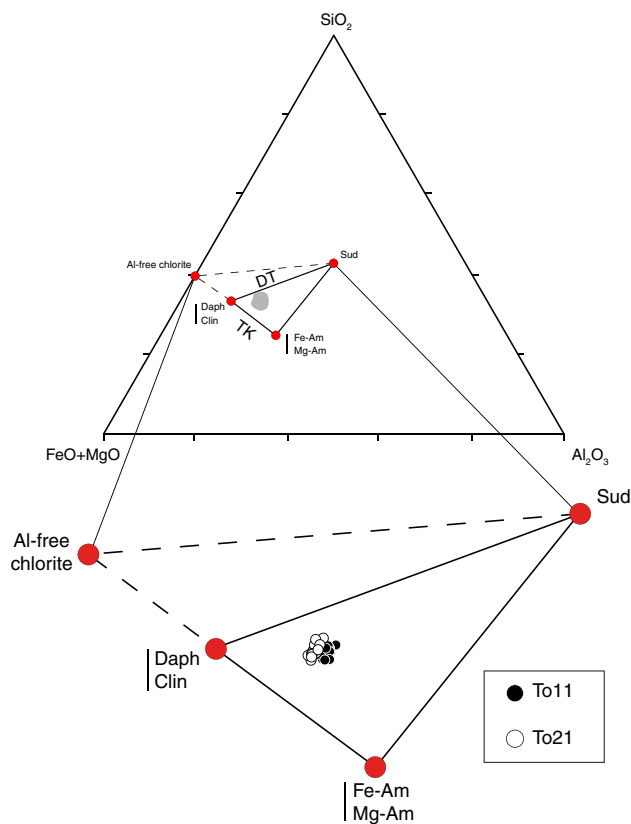


Fig. 8 FeMg-Si-Al ternary plot presenting the newly formed chlorite compositional data from analyzed S_{V2} veins (samples To11 and To21). Chlorite end-member composition of Vidal et al. (2001) and Inoue et al. (2009) have also been reported. *Sud* sudoite, *Fe-Am*, Fe-amesite; *Mg-Am*, Mg-amesite; *Daph*, daphnite; *Clin*, clinoclchlore

Table 4 $\delta^{18}\text{O}$ and δD values of clay fractions ($<2\ \mu\text{m}$), hand-picked chlorite crystals, and quartz from E_{V2} veins

Sample	Rock	Mineral	Sampling site	$\delta^{18}\text{O}$ (‰)	δD (‰)
To17	Limestone	Clay fractions	Hanging wall	21.7	-65
To06	Deformed marls	Clay fractions	Fault	19.3	-72
To19	Deformed marls	Clay fractions	Fault	19.2	-68
To34	Pelite	Clay fractions	Footwall	17.9	-88
To21	Deformed marls	Chlorite	Fault	17.5	-66
To11	Deformed marls	Chlorite	Fault	17	-
To11	Deformed marls	Quartz	Fault	25.5	-
To11	Deformed marls	Quartz	Fault	25.1	-

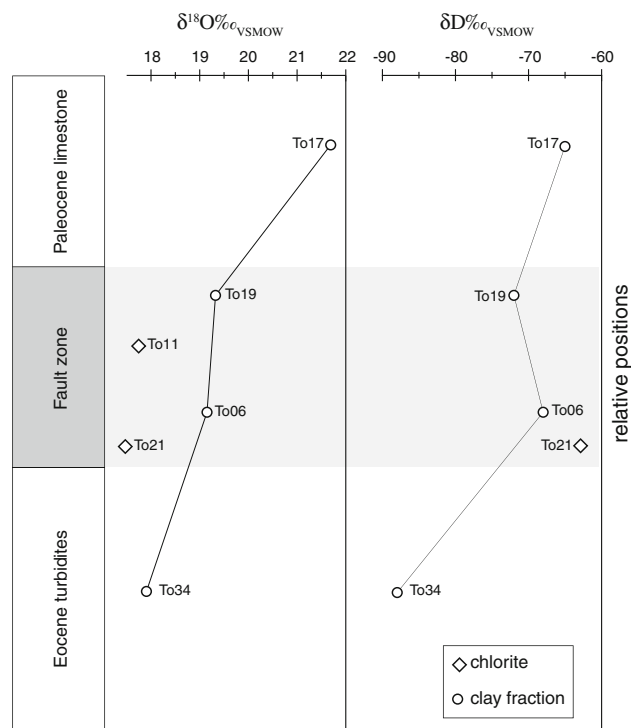


Fig. 9 $\delta^{18}\text{O}$ and δD values of $<2\ \mu\text{m}$ clay fractions (white circles) and hand-picked chlorite crystals (white diamonds) according to their relative structural position

between 17.9 and 21.7‰, with the higher values for sample from the Alveolina limestone and the lower values for the pelitic host rocks (Table 4 and Fig. 9). In the fault zone, the $\delta^{18}\text{O}$ values of $<2\ \mu\text{m}$ fraction are intermediate (about 19.3‰). In the host sediments, δD values are between -88 and -65 ‰ with higher values for samples from the Alveolina limestone and lower values for pelites, respectively. The two samples from the fault zone have similar δD values of about -70 ‰, intermediate between the values measured on clays from the two non-deformed rocks.

Hand-picked chlorite crystals from S_{V2} veins from sample To21 and To11 have $\delta^{18}\text{O}$ values between 17 and 17.5‰. The δD value for the latter mineral was measured in sample To21 and is -66 ‰ (Table 4 and Fig. 9).

The $\delta^{18}\text{O}$ values of quartz cements from E_{V2} veins (sample To21) are 25.1 and 25.5‰ (Table 4).

Discussion

Behavior and origin of phyllosilicates during deformation

The presence of illite and chlorite and the absence of expandable clays such as smectite in clay fractions from the host sediments (hanging wall limestone and footwall

turbidites) suggest that the sediment has experienced a high grade of diagenesis.

Chlorite-mica aggregates of various sizes are present in the pelite and sandstone host rocks. These observations are consistent with the study of Bauluz Lázaro et al. (2008), who described similar clay assemblages in the Hecho group turbidites located further south in the Jaca basin. According to these authors, the chlorite-illite aggregates are interpreted to have a detrital origin derived from the low-grade metamorphic basement rocks (Hercynian basement) outcropping in the foreland margin during the Hecho group sedimentation (Mansurbeg et al. 2009). The large detrital chlorite-mica aggregates (>10 μm) in the matrix of host sediments can either be accumulated along pressure-solution surfaces as an “insoluble residue” or be bedding-parallel. This suggests that the slaty cleavage in host sediments is mainly established in the passive form, where detrital illite-chlorite stacks are reoriented mechanically, a process that has been assisted by removal of calcite along pressure-solution surfaces (Kreutzberger and Peacor 1988; Li et al. 1994; and Ho et al. 2001).

The intensely deformed fault zone is characterized by a pervasive cleavage with preferential orientation of phyllosilicates. The mechanisms of cleavage formation can be either mechanical reorientation of pre-existing grains or recrystallization depending on the diagenetic or metamorphic grade (Lee et al. 1986; Kreutzberger and Peacor 1988; and Ho et al. 2001). Lacroix et al. (2011) have also shown that calcite and quartz dissolution occurs along cleavage planes. The chemical transfer process is favored by the abundance of illite and the small size of quartz and calcite grains exposed to dissolution in the deformed sediment, both features being known to increase the rate of pressure solution (e.g., Bos et al. 2000; Renard et al. 2000; Solum and Van der Pluijm 2009).

The intensely deformed sediments have a higher proportion of chlorite in <2 μm as well as in 2–16 μm clay fractions compared to the host sediments (Alveolina limestone from hanging wall and Hecho group turbidites from footwall). This is confirmed by the presence of newly formed chlorite with a high iron content along S_V2 microveins.

Origin of fluids

In a previous study of the Monte Perdido thrust fault, Lacroix et al. (2011) evidence that calcite from S_V1 veins (related to the first stage of deformation) is in equilibrium with calcite from deformed and host sediments. The $\delta^{13}\text{C}$ values from fault zone and calcite veins are compatible with precipitation from fluids directly derived from or buffered by the rocks of the adjacent hanging and footwall.

The $\delta^{18}\text{O}$ and δD values of <2 μm clay fractions from the deformed zone are intermediate to those measured on clays from the two non-deformed rocks (hanging wall Alveolina limestone and footwall turbidites). The clear evidence of newly formed phyllosilicates, with for example the precipitation of chlorite along S_V2 veins, supports a partial dissolution and recrystallisation of clay minerals during deformation. The intermediate isotopic composition for clays in the fault zone rocks compared to their host sediments indicates a closed-system fluid circulation where the fluid isotopic composition was buffered by the host rocks. In such a closed system, the fluids could have remained essentially static, with solutes being transported by diffusion, or fluid transfer occurring over limited distances only from both the hanging wall and footwall toward the fault zone.

δD values of clay minerals can provide direct information about those of the fluid. Such estimates are valid only if the chlorite or clay cements from the S_V2 veins have not re-equilibrated after precipitation. According to the studies of closure temperatures for hydrogen diffusion in chlorite of Graham et al. (1987), closure temperatures ranging from 270°C up to more than 500°C with cooling rate varying from 1 to 4°C/Ma can be estimated for 100 μm thick chlorite. In the present case, the Monte Perdido thrust fault reached a maximum temperature of 240°C (see below). The fault activity was dated from –47 to –37 Ma (Mutti et al. 1988) and consequently was exhumed at a cooling rate higher than 5°C/Ma. With such a cooling rate, hydrogen isotope exchange with a hydrous fluid or other minerals is not expected. As oxygen isotope exchange at any given temperature is generally slower compared to hydrogen (e.g., Sharp 2009), the preservation of oxygen isotope compositions of the minerals can also be expected. For the Monte Perdido P–T and cooling rate conditions, the oxygen and hydrogen isotope composition of newly formed chlorite in the S_V2 veins may hence be used to determine those of the fluid. Chlorite in the S_V2 veins has δD values between –88 and –65‰ and $\delta^{18}\text{O}$ values between 17.9 and 21.7‰ (Fig. 10). These values are typical of those for minerals in sedimentary rocks that generally range from 8 to 25‰ for oxygen and from –100 to –30‰ for hydrogen (Longstaffe 1987; Longstaffe et al. 2003; Sharp 2009). Using the oxygen isotope fractionations determined by Cole and Ripley (1998), the mineralizing fluid from which chlorite precipitated have $\delta^{18}\text{O}$ values of between 14.4 and 16.3‰ (1 in Fig. 10), within the range typical for formation water compositions (Longstaffe 1987; Sharp 2009). For hydrogen, the chlorite–water calibration of Graham et al. (1987) was chosen. The δD values of the fluid are hence calculated to be –36 to –26‰ (2 in Fig. 10). These results also suggest that the chlorite and clay fractions were formed from formation water. Although slightly higher in

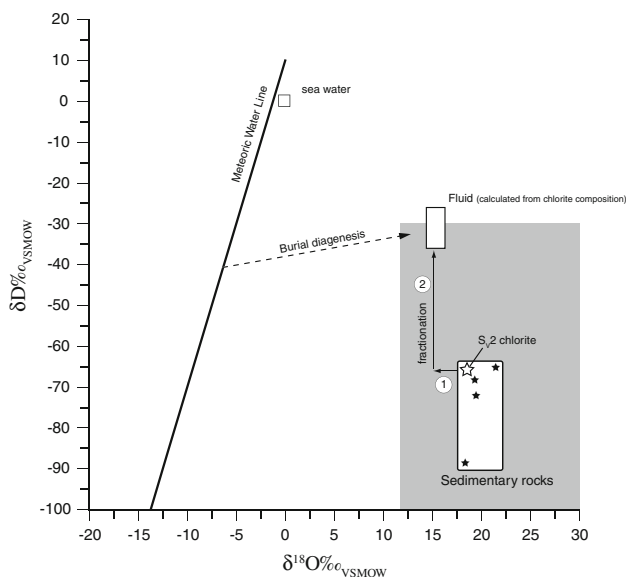


Fig. 10 Plot of δD vs. $\delta^{18}O$ values of clay fractions (black stars) and hand-picked chlorite crystals (white star) samples from the hanging wall, footwall, and fault zone. Sedimentary rock compositions are from Sharp (1999). Dashed arrow shows an example of the original fluid composition trapped in the pores and re-equilibrated with sediments during burial diagenesis. Fluid composition was calculated from pure chlorite composition. 1 and 2 are, respectively, the O and H isotope fractionation between pure chlorite and water using the Cole and Ripley (1998) and Graham et al. (1987) fractionation curves

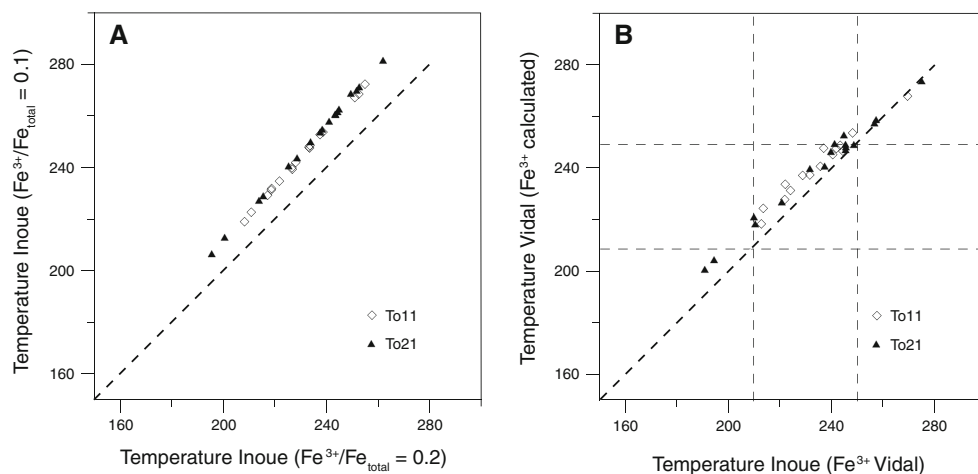
^{18}O -content, this fluid composition is consistent with that determined by Lacroix et al. (2011). The different burial depths between S_V1 and S_V2 veins formation, with S_V2 veins formed at deeper conditions (see below), can explain the difference observed in oxygen isotope composition. The formation water corresponds to fluid present in the pore space of the sediment and, as suggested in the Fig. 10, may have been derived from mixed meteoric-seawater sources, but was likely continually re-equilibrated with sediments during burial diagenesis (e.g., Longstaffe 1987).

Conditions of deformation–temperature calculation

The “Illite crystallinity” (IC) is often used to determine the temperature of clay mineral formation and hence help constrain the degree of diagenesis and low-grade metamorphism (Lee et al. 1986; Essene and Peacor 1995; Ji and Browne 2000; and Kübler and Jaboyedoff 2000). However, because IC may also be influenced by the origin of detrital illite, this parameter cannot be used for the Monte Perdido thrust fault. Therefore, other approaches were used: compositional chlorite geothermometry and stable isotope thermometry.

In order to describe the numerous substitutions of chlorite mentioned above, appropriate end-member components have to be selected. The composition of the newly formed chlorite along S_V2 micro-veins can be expressed as the activities of end-member components described either by Vidal et al. (2006) or by Inoue et al. (2009) (Fig. 8). The choice of their components represents the Fe-Mg, Tschermak, and dioctahedral-trioctahedral substitutions occurring in trioctahedral chlorites. These two geothermometers were thus used to calculate temperatures of formation. Significant amounts of Fe^{3+} can influence the number of vacancies in the chlorite structure, and hence, Fe^{3+} should be taken into consideration when estimating the temperature of formation. Inoue et al. (2009) demonstrated that neglecting the presence of ferric iron in chlorite causes a serious error for the estimation of the formation temperatures of chlorites in rocks of diagenetic-hydrothermal origin. To use the model developed by Inoue et al. (2009), the $Fe^{3+}/(Fe^{3+}+Fe^{2+})$ was taken to be equal to 0.2 and 0.1, values generally applicable to diagenetic chlorites. Temperatures calculated by the model developed by Inoue et al. (2009) range from 195 to 280°C. Temperatures are slightly higher for lower Fe^{3+} proportions, with a mean value at 230 and 245°C for $Fe^{3+}/(Fe^{3+}+Fe^{2+}) = 0.2$ and 0.1, respectively (Table 3, Fig. 11a). Temperatures calculated

Fig. 11 Plots of estimated temperatures for the formation of chlorite in S_V2 veins. **a** Comparison of estimated temperature using the thermodynamic model of Inoue et al. (2009) with $Fe^{3+}/Fe^{3+}+Fe^{2+} = 0.2$ and 0.1. **b** Comparison of estimated temperatures calculated using models of Vidal et al. (2005) and Inoue et al. (2009)



by the model developed by Vidal et al. (2005, 2006) range from 205 to 280°C, with a mean value at 240°C (Table 3, Fig. 11b). A simultaneous estimation of $X(\text{Fe}^{3+})$ in chlorite has been done using a criteria based on the convergence of equilibria. These minimal values of $X(\text{Fe}^{3+})$ are required to obtain convergence of Eq. 1–Eq. 4. Higher Fe^{3+} values are possible without losing this convergence. Values obtained are specified in Table 3 and are between 0.05 and 0.23. Figure 11b shows the very good correlation between temperatures derived from Inoue's thermometer, using $X(\text{Fe}^{3+})$ content estimated with Vidal et al. (2006) thermodynamic data, and temperatures estimated with the Vidal et al. (2006) thermometer.

The second approach consists of a temperature estimate based on stable isotope compositions of a pair of minerals and assuming that: (1) both minerals were formed together, (2) fractionation factors are available for both minerals, and (3) they did not re-equilibrate with each other or with other phases during cooling after first formation.

Microstructural analyses indicate that quartz in the E_{V2} veins is coeval with chlorite from the S_{V1} veins. Assuming that these minerals were formed in isotopic equilibrium with the same fluid, it is possible to use the available fractionation factors and determine their temperature of formation.

A number of calibrations for oxygen isotope fractionation factors have been published for chlorite- H_2O (i.e., Wenner and Taylor 1971; Savin and Lee 1988; Zheng 1993; Buatier et al. 1995 and Cole and Ripley 1998) and quartz- H_2O (Shiro and Sakai 1972; Bottinga and Javoy 1975; Matsuhisa et al. 1979; Zhang et al. 1989; Zheng 1993; and Sharp and Kirschner 1994). These calibrations have been determined using four approaches: laboratory equilibrium experiments, statistical mechanical calculations, empirical estimates based on the isotopic compositions of natural samples, and calculations based on empirical bond-type models. Because of slow exchange rates and possible isotopic disequilibrium during experimental conditions, there are no experimental calibrations of chlorite-water fractionation factors at low temperatures (i.e. <350°C). Moreover, the calibration curves are likely to apply chlorite of restricted chemical composition only. In this study, the calibration by Cole and Ripley (1998) was chosen for chlorite-water. The latter was determined for Fe-Mg chlorite with a similar composition to those studied here and was calibrated over a similar temperature range (from 150 to 350°C) as that of interest to the present study.

For quartz, Zhang et al. (1989) have determined experimentally the oxygen isotope fractionation between quartz and water. Subsequent work by Zheng (1993), based on empirical bond-type models, has confirmed the validity of this experimental calibration. Given the good agreement

between both approaches, the fractionation factor from Zhang et al. (1989) was hence used in conjunction with the chlorite-water fractionation to determine temperatures of E_{V2} vein formation:

$$1000 \ln \alpha_{\text{qtz-chl}} = -2.693 \cdot \frac{10^9}{T^3} + 9.648 \cdot \frac{10^6}{T^2} - 2.969 \cdot \frac{10^3}{T} - 2.71$$

(with $1000 \ln \alpha \approx \delta^{18}\text{O}_{\text{qtz}} - \delta^{18}\text{O}_{\text{chl}}$)

The $\delta^{18}\text{O}$ values of quartz and chlorite give a $\Delta_{\text{qtz-chl}}$ of between 7.8 and 8.3‰. Equation 10 predicts a temperature of cogenetic quartz and chlorite formation of 234–265°C.

The different approaches based on the chemical and isotopic composition of chlorite provide a similar temperature range. The slightly higher temperatures determined with the isotopic approach may be attributed to slight compositional differences of chlorite and the effects of this on the oxygen isotope fractionation factor (Cole and Ripley, 1998). However, the temperature estimates do overlap within their analytical errors, attesting that these methods constitute good alternatives to determine temperature in this diagenetic context.

Conditions of deformation—pressure and burial estimates

From micro-thermometric data on fluid inclusions, Lacroix et al. (2011) determined two isochores related to the precipitation of the S_{V1} shear veins and E_{V2} extension veins (Fig. 12).

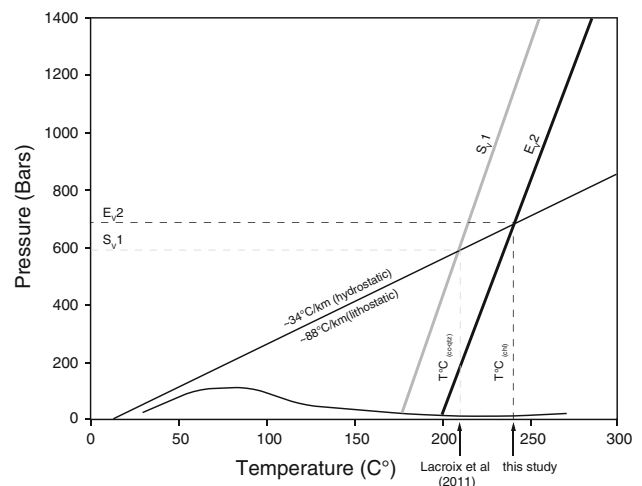


Fig. 12 Temperature–pressure diagram illustrating the conditions of S_{V1} and E_{V2} veins as inferred from fluid inclusions (modified from Lacroix et al. 2011). *Gray line*: isochore for primary fluid inclusions in S_{V1} veins. *Black line*: isochore for primary inclusions in E_{V2} veins. The temperature of 240°C was calculated from thermodynamic models of Vidal et al. (2001, 2005) and Inoue et al. (2009). This new data confirms the geothermal gradient deduced in Lacroix et al. (2011) on S_{V1} veins (plotted in *gray* for comparison)

They constrained a pressure of ~ 570 bars related to the first stage of deformation (S_{V1} veins formation) using a temperature of about 210°C calculated with oxygen isotopic composition of cogenetic calcite and quartz minerals. These P–T conditions are in agreement with a hydrostatic geothermal gradient of $34^{\circ}\text{C}/\text{km}$.

In order to constrain the P–T conditions during the second stage of deformation, the isochores for E_{V2} extension veins determined from fluid inclusions in quartz by Lacroix et al. (2011) are combined with new temperatures calculated from chlorite thermometry and stable isotope compositions (Fig. 12). A mean value of 240°C is used to constrain the related pressure condition of formation by projecting the plot of the calculated temperature interval on the appropriate isochore. Thus, a fluid pressure of about 700 bars is estimated for S_{V2} and E_{V2} vein formation. Such a P–T domain is very close to the hydrostatic geothermal gradient of about $34^{\circ}\text{C}/\text{km}$ determined by Lacroix et al. (2011) using calcite and quartz precipitated during the first stage of deformation. In the study of the Pineta thrust fault, located a few kilometers northward from our study area, Rye and Bradbury (1988) determined a similar geothermal gradient of about $32^{\circ}\text{C}/\text{km}$. Moreover, this geothermal gradient of $32^{\circ}\text{C}/\text{km}$ is close to the modern geothermal gradient of $30^{\circ}\text{C}/\text{km}$ that affects the Pyrenean axial zone (Zeyen and Fernández 1994).

The P–T conditions determined here assume a hydrostatic fluid pressure even if previous studies (Hubbert and Rubey 1959; Sibson 1985) indicate that thrust faults are expected to move under near lithostatic fluid pressure. Values close to lithostatic fluid pressure recorded in mineralization is unrealistic during the Monte Perdido thrust activity since it would imply a geothermal gradient of up to $100^{\circ}\text{C}/\text{km}$ and an overburden sediment thickness of only ~ 2 km. Mutti et al. (1988) and Remacha and Fernandez (2003) estimated that the overburden sediment thickness was up to 5,000 m during the Monte Perdido thrusting. Moreover, the hypothesis of a hydrostatic fluid pressure during mineral precipitation is coherent with the model proposed by Wiltschko et al. (2009), where thrust fault movement requires near lithostatic fluid pressure, and mineral precipitation could record lower hydrostatic fluid pressure.

The present study thus supports a reactivation of the Monte Perdido thrust fault at a burial depth of about 7 km involving newly formed chlorite in S_{V2} veins. This fault reactivation is probably associated to the emplacement of the underlying Gavarnie thrust unit (Priabonian—early Oligocene), at deeper burial conditions than the initial emplacement of the Monte Perdido thrust unit (Meresse 2010).

Conclusions

The present study demonstrates that the behavior and transformation of clay minerals is of major importance and can provide essential information about the temperature and burial conditions during the fault activity.

1. In the hanging wall and footwall, cleavage development was mainly driven by pressure solution and mechanical reorientation of chlorite-mica aggregates.
2. The fault zone is characterized by a pervasive cleavage with a preferential orientation of small illite particles and the presence of newly formed iron-rich chlorite crystals along S_{V2} micro-veins.
3. The wide range of IC measured in the fault zone is attributed to heterogeneous origins of illite grains along the Monte Perdido thrust fault. Therefore, IC data cannot be used to establish the conditions of deformation.
4. Authigenic clay minerals in the fault zone precipitated from formation water directly derived from the local hanging wall and footwall rocks, or fluids that were buffered by these rocks. Under these conditions, the mineralization observed in the thrust faults recorded the P–T conditions of thrust activity.
5. Compositional chlorite geothermometry and stable isotope thermometry are found to give a similar range of temperature conditions, validating the use of both thermometers for studies of this type. Given the chlorite compositions, the Vidal et al. (2001, 2005) and Inoue et al. (2009) equations give similar temperature range with a mean value of 240°C . The O-isotope fractionation between cogenetic chlorite (S_{V2} veins) and quartz (E_{V2} veins) gives temperatures of 234 – 265°C .
6. A burial of about 7 km is necessary to obtain temperatures estimated from S_{V2} veins formed during the Monte Perdido thrust fault reactivation. These temperature–burial conditions are consistent with a geothermal gradient of about $34^{\circ}\text{C}/\text{km}$.

Finally, the Monte Perdido thrust fault was formed during two stages. The first stage was related to the Monte Perdido thrust unit emplacement associated to the formation of S_{V1} calcite-quartz shear veins at a temperature of about 210°C . The second stage consists of a reactivation of the thrust fault at higher temperature and pressure. During this stage, the behavior and transformation of clay minerals are of major importance. We demonstrate that clay minerals can be valuable low-grade geothermometers.

Acknowledgments This work was realized within the framework of the 3F “Fault, Fluid, Flow” program funded by INSU-CNRS. We thank Nicolas Rouge from the University of Franche Comté (Besançon) for SEM technical support and Benita Putlitz from the University of Lausanne for discussion and analytical support on

oxygen isotope analysis. We also thank Olivier Vidal, an anonymous reviewer, and Franck Poitrasson (CMP Associate Editor) for their constructive reviews improving the manuscript.

References

- Aadate T, Stinnesbeck W, Keller G (1996) Lithologic and mineralogic correlations of near K/T boundary clastic sediments in NE Mexico: Implication for origin and nature of deposition. Sp. publications. Soc Geol Am 307:211–226
- Alavi M (2004) Regional stratigraphy of the Zagros fold-thrust belt of Iran and its proforeland evolution. Am J Sci 304:1–20
- Bauluz Lázaro B, González López JM, Yuste Oliete A, Mayayo Burillo MJ (2008) Evolución Diagenética de las Turbiditas del Grupo Hecho (Eoceno) en la Cuenca de Jaca (España), SEM 2008, Zaragoza
- Beaumont C, Muñoz JA, Hamilton J, Fullsack P (2000) Factors controlling the Alpine evolution of the central Pyrenees inferred from a comparison of observations and geodynamical models. J Geophys Res 105(B4):8121
- Berman RG (1988) Internally-consistent thermodynamic data for minerals in the system Na₂O–K₂O–CaO–MgO–FeO–Fe₂O₃–Al₂O₃–SiO₂–TiO₂–H₂O–CO₂. J Petrol 29:445–522
- Bos B, Peach CJ, Spiers CJ (2000) Frictional-viscous flow of simulated fault gouge caused by the combined effects of phyllosilicates and pressure solution. Tectonophysics 327:173
- Bottinga Y, Javoy M (1975) Oxygen isotope partitioning among the minerals in igneous and metamorphic rocks. Rev Geophys 13:401–418
- Buatier MD, Früh-Green GL, Karpoff AM (1995) Mechanisms of Mg-phyllosilicate formation in a hydrothermal system at a sedimented ridge (Middle Valley, Juan de Fuca). Contrib Mineral Petrol 122:134
- Caja MA, Marfil R, Garcia D, Remacha E, Morad S, Mansurbeg H, Amorosi A, Martínez-Calvo C, Lahoz-Beltrá R (2009) Provenance of siliciclastic and hybrid turbiditic arenites of the Eocene Hecho Group, Spanish Pyrenees: implications for the tectonic evolution of a foreland basin. Basin Res 22(2):157
- Cathelineau M (1988) Cation site occupancy in chlorites and illites as a function of temperature. Clay Minerals 23(4):471–485
- Cathelineau M, Nieva D (1985) A chlorite solid solution geothermometer the Los Azufres (Mexico) geothermal system. Contrib Mineral Petrol 91(3):235
- Choukroune P, Roure F, Pinet B (1990) Main results of the ECORS Pyrenees profile. Tectonophysics 173(1–4):411
- Cole DR, Ripley EM (1998) Oxygen isotope fractionation between chlorite and water from 170 to 350°C: a preliminary assessment based on partial exchange and fluid/rock experiments. Geochim Cosmochim Acta 63(3–4):449
- Day-Stirrat RJ, Aplin AC, Srodon J, Van der Pluijm BA (2008) Diagenetic reorientation of phyllosilicate minerals in paleogene mudstones of the Podhale basin, southern Poland. Clays Clay Minerals 56(1):100–111
- De Caritat P, Hutcheon I, Walshe JL (1993) Chlorite geothermometry; a review. Clays Clay Minerals 41(2):219–239
- Durney DW, Ramsay JG (1973) Incremental strains measured by syntectonic crystal growth. Gravity Tectonics 67–96
- Essene EJ, Peacor DR (1995) Clay mineral thermometry; a critical perspective. Clays Clay Minerals 43(5):540–553
- Frey, M (1987) Very low-grade metamorphism of clastic sedimentary rocks: in low temperature metamorphism. In: Frey M (ed) Chapman and Hall, New York, pp 9–58
- Graham CM, Vigliano JA, Harmon RS (1987) Experimental study of hydrogen-isotope exchange between aluminous chlorite and water and of hydrogen diffusion in chlorite. Am Mineral 72:566–579
- Hillier S, Velde B (1991) Octahedral occupancy and chemical composition of diagenetic (low-temperature) chlorites. Clay Minerals 26:149–168
- Ho NC, van der Pluijm BA, Peacor DR (2001) Static recrystallization and preferred orientation of phyllosilicates: Michigan formation, northern Michigan, USA. J Struct Geol 23:887
- Holl JE, Anastasio DJ (1995) Cleavage development within a foreland fold and thrust belt, southern Pyrenees, Spain. J Struct Geol 17:357–369
- Hubbert MK, Rubey WW (1959) Role of fluid pressure in mechanics of overthrust faulting. Geol Soc Am Bull 70:115–166
- Inoue A, Meunier A, Patrier-Mas P, Rigault C, Beaufort D, Vieillard P (2009) Application of chemical geothermometry to low-temperature trioctahedral chlorites. Clays Clay Minerals 57:371–382
- Ji J, Browne PRL (2000) Relationship between illite crystallinity and temperature in active geothermal systems of New Zealand. Clays Clay Minerals 48:139–144
- Kasemann S, Meixner A, Rocholl A, Vennemann T, Rosner M, Schmitt AK, Wiedenbeck M (2001) Boron and oxygen isotope composition of certified reference materials NIST SRM 610/612 and reference materials JB-2 and JR-2. Geostandards Newslett 25:405
- Kirschner DL, Sharp ZD, Masson H (1995) Oxygen isotope thermometry of quartz-calcite veins: unraveling the thermal-tectonic history of the subgreenschist facies Morcles nappe (Swiss Alps). Geol Soc Am Bull 107:1145–1156
- Kreutzberger ME, Peacor DR (1988) Behavior of illite and chlorite during pressure solution of shaly limestone of the Kalkberg formation, Catskill, New York. J Struct Geol 10:803
- Kübler B (1964) Les argiles, indicateurs de métamorphisme. Rev Inst Franc Pétrole 19:1093–1112
- Kübler B (1987) Cristallinité de l'illite, méthodes normalisées de préparations, méthodes normalisées de mesures. Cahiers Institut Géologie de Neuchâtel, Suisse, série ADX
- Kübler B, Jaboyedoff M (2000) Illite crystallinity CONCISE REVIEW PAPER. Comptes Rendus de l'Académie des Sciences—Series IIA—Earth and Planetary Science 331:75
- Labaume P, Seguret M, Seyve C (1985) Evolution of a turbiditic foreland basin and analogy with an accretionary prism: example of the Eocene South-Pyrenean Basin. Tectonics 4:661–685
- Lacroix B, Buatier M, Labaume P, Travé A, Dubois M, Charpentier D, Ventalon S, Convert-Gaubier D (2011) Microtectonic and geochemical characterization of thrusting in a foreland basin: example of the South-Pyrenean orogenic wedge (Spain). J Struct Geol 33:1359–1377
- Lee JI, Lee YI (2001) Kubler illite “crystallinity” index of the Cretaceous Gyeongsang Basin, Korea: implications for basin evolution. Clays Clay Minerals 49(1):36–43
- Lee JH, Peacor DR, Lewis DD, Wintch RP (1986) Evidence for syntectonic crystallization for the mudstone to slate transition at Lehigh gap, Pennsylvania, USA. J Struct Geol 8:767
- Li G, Peacor DR, Merriman RJ, Roberts B, Van der Pluijm BA (1994) TEM and AEM constraints on the origin and significance of chlorite-mica stacks in slates: an example from Central Wales, UK. J Struct Geol 16:1139
- Longstaffe FJ (1987) Stable isotope studies of diagenetic studies. Mineralogical Association of Canada. Short Course 13:225–262
- Longstaffe FJ, Calvo R, Ayalon A, Donaldson S (2003) Stable isotope evidence for multiple fluid regimes during carbonate cementation of the Upper Tertiary Hazeva formation, Dead Sea Graben, southern Israel. J Geochem Explor 80:151–170
- Macgregor DS (1996) Factors controlling the destruction or preservation of giant light oilfields. Petrol Geosci 2:197–217

- Mansurbeg H, Caja MA, Marfil R, Morad S, Remacha E, Garcia D, Martin-Crespo T, El-Ghali MAK, Nystuen JP (2009) Diagenetic evolution and porosity destruction of Turbiditic Hybrid Arenites and Siliciclastic Sandstones of Foreland Basins: evidence from the Eocene Hecho Group, Pyrenees, Spain. *J Sed Res* 79:711–735
- Matsuhisa Y, Goldsmith JR, Clayton RN (1979) Oxygen isotopic fractionation in the system quartz-albite-anorthite-water. *Geochim Cosmochim Acta* 43:1131
- Meresse F (2010) Dynamique d'un prisme orogénique intracontinental: évolution thermochronologique (traces de fission sur apatite) et tectonique de la Zone Axiale et des piedmonts des Pyrénées centro-occidentales. University of Montpellier, Dissertation 2
- Merriman RJ, Roberts B, Peacor DR, Hirons SR (1995) Strain-related differences in the crystal growth of white mica and chlorite: a TEM and XRD study of the development of metapelitic microfabrics in the Southern Uplands thrust terrane, Scotland. *J Metamorphic Geol* 13:559
- Moore DM, Reynolds RC (1997) X-ray diffraction and the identification and analysis of clay minerals. Oxford University Press, Oxford
- Munoz JA (1992) Evolution of a continental collision belt: ECORS-Pyrenees crustal balanced cross-section. In: McClay K (ed) Thrust tectonics, pp 235–246
- Mutti E, Séguret M, Sgavetti M (1988) Sedimentation and deformation in the Tertiary sequences of the Southern Pyrenees. Field Trip 7 guidebook, AAPG Mediterranean Basins Conference, Nice, France (Special Publication of the Institute of Geology of the University of Parma, Parma, Italy)
- Oliva-Urcia B, Larrasoña JC, Pueyo EL, Gil A, Mata P, Parés JM, Schleicher AM, Pueyo O (2009) Disentangling magnetic subfabrics and their link to deformation processes in cleaved sedimentary rocks from the Internal Sierras (west central Pyrenees, Spain). *J Struct Geol* 31:163
- Parry WT, Blamey NJF (2010) Fault fluid composition from fluid inclusion measurements, Laramide age Uinta thrust fault, Utah. *Chem Geol* 278:105
- Remacha E, Fernandez LP (2003) High-resolution correlation patterns in the turbidite systems of the Hecho group (South-Central Pyrenees, Spain). *Marine Petrol Geol* 20:711–726
- Renard F, Gratier JP, Jamtveit B (2000) Kinetics of crack-sealing, intergranular pressure solution, and compaction around active faults. *J Struct Geol* 22:1395
- Roure F, Sassi W (1995) Kinematics of deformation and petroleum system appraisal in Neogene foreland fold-and-thrust belts. *Petrol Geosci* 1:253–269
- Rumble D, Hoering TC (1994) Analysis for oxygen and sulfur isotope ratios in oxide and sulfide minerals by spot heating with a carbon dioxide laser in a fluorine atmosphere. *Acc Chem Res* 27:237
- Rye DM, Bradbury HJ (1988) Fluid flow in the crust; an example from a Pyrenean thrust ramp. *Am J Sci* 288:197–235
- Savin SM, Lee M (1988) Isotopic studies of phyllosilicates. *Rev Mineral Geochem* 19:189–223
- Schwartz S, Tricart P, Lardeaux JM, Guillot S, Vidal O (2009) Late tectonic and metamorphic evolution of the Piedmont accretionary wedge (Queyras Schistes lustrés, western Alps): evidences for tilting during Alpine collision. *Geol Soc Am Bull* 121:502–518
- Séguret M (1972) Etude tectonique des nappes et séries décollées de la partie centrale du versant sud des Pyrénées. Publications de l'Université des Sciences et Technologiques du Languedoc (Ustela)
- Sharp ZD (1990) A laser-based microanalytical method for the in situ determination of oxygen isotope ratios of silicates and oxides. *Geochim Cosmochim Acta* 54:1353
- Sharp ZD (2009) Application of stable isotope geochemistry to low-grade metamorphic rocks, Blackwell Publishing Ltd., p 227
- Sharp ZD, Kirschner DL (1994) Quartz-calcite oxygen isotope thermometry: a calibration based on natural isotopic variations. *Geochim Cosmochim Acta* 58:4491
- Sharp ZD, Atudorei V, Durakiewicz T (2001) A rapid method for determining the hydrogen and oxygen isotope ratios from water and solid hydrous substances. *Chem Geol* 178:197–210
- Shiro Y, Sakai H (1972) Calculation of the reduced partition function ratios of alpha-beta quartz and calcite. *Jap Chem Soc Bull* 45:2355–2359
- Sibson RH (1985) A note on fault reactivation. *J Struct Geol* 7:751–754
- Solum JG, van der Pluijm BA (2009) Quantification of fabrics in clay gouge from the Carboneras fault, Spain and implications for fault behavior. *Tectonophysics* 475:554
- Teixell A (1996) The Anso transect of the southern Pyrenees: basement and cover thrust geometries. *J Geol Soc* 301–310
- Teixell A (1998) Crustal structure and orogenic material budget in the west central Pyrenees. *Tectonics* 17:395
- Vidal O, Parra T, Trotet F (2001) A thermodynamic model for Fe–Mg aluminous chlorite using data from phase equilibrium experiments and natural pelitic assemblages in the 100° to 600°C, 1–25 kb range. *Am J Sci* 301:557–592
- Vidal O, Parra T, Vieillard P (2005) Thermodynamic properties of the Tschermak solid solution in Fe-chlorite: application to natural examples and possible role of oxidation. *Am Mineral* 90:347–358
- Vidal O, De Andrade V, Lewin E, Munoz M, Parra T, Pascarelli S (2006) P–T-deformation-Fe₃₊/Fe₂₊ mapping at the thin section scale and comparison with XANES mapping: application to a garnet-bearing metapelite from the Sambagawa metamorphic belt (Japan). *J Metam Geol* 24:669–683
- Wenner DB, Taylor HP (1971) Temperatures of serpentinization of ultramafic rocks based on O¹⁸/O¹⁶ fractionation between coexisting serpentine and magnetite. *Contrib Mineral Petrol* 32(3):165
- Wiltchko DV, Lambert GR, Lamb W (2009) Conditions during syntectonic vein formation in the footwall of the Absaroka Thrust Fault, Idaho-Wyoming-Utah fold and thrust belt. *J Struct Geol* 31(9):1039
- Zane A, Sassi R, Guidotti CV (1998) New data on metamorphic chlorite as a petrogenetic indicator mineral, with special regard to greenschist-facies rocks. *Can Mineral* 36:713–726
- Zeyen H, Fernández M (1994) Integrated lithospheric modeling combining thermal, gravity, and local isostasy analysis: application to the NE Spanish geotranssect. *J Geophys Res* 99(B9):180–189
- Zhang LG, Liu JX, Zhou HB, Chen ZS (1989) Oxygen isotope fractionation in the quartz-water-salt system. *Econ Geol* 89:1643–1650
- Zheng YF (1993) Calculation of oxygen isotope fractionation in anhydrous silicate minerals. *Geochim Cosmochim Acta* 57:1079